Supplementary Materials

Interdecadal Pacific Oscillation responsible for the linkage of decadal changes in precipitation/moisture in arid central Asia and humid Asian monsoon region during the last millennium

Hongna Xu[1], Tao Wang[1,2,*], Huijun Wang[1,2]

[1] Collaborative Innovation Center on Forecast and Evaluation of Meteorological Disasters (CIC-FEMD), Nanjing University of Information Science and Technology, Nanjing 210044, China

[2] Climate Change Research Center and Nansen-Zhu International Research Centre, Institute of Atmospheric Physics, Chinese Academy of Sciences, Beijing 100029, China

* Corresponding author: Tao Wang (wangtao@mail.iap.ac.cn)

List of Supplementary Materials:

Supplementary Figures 1–13

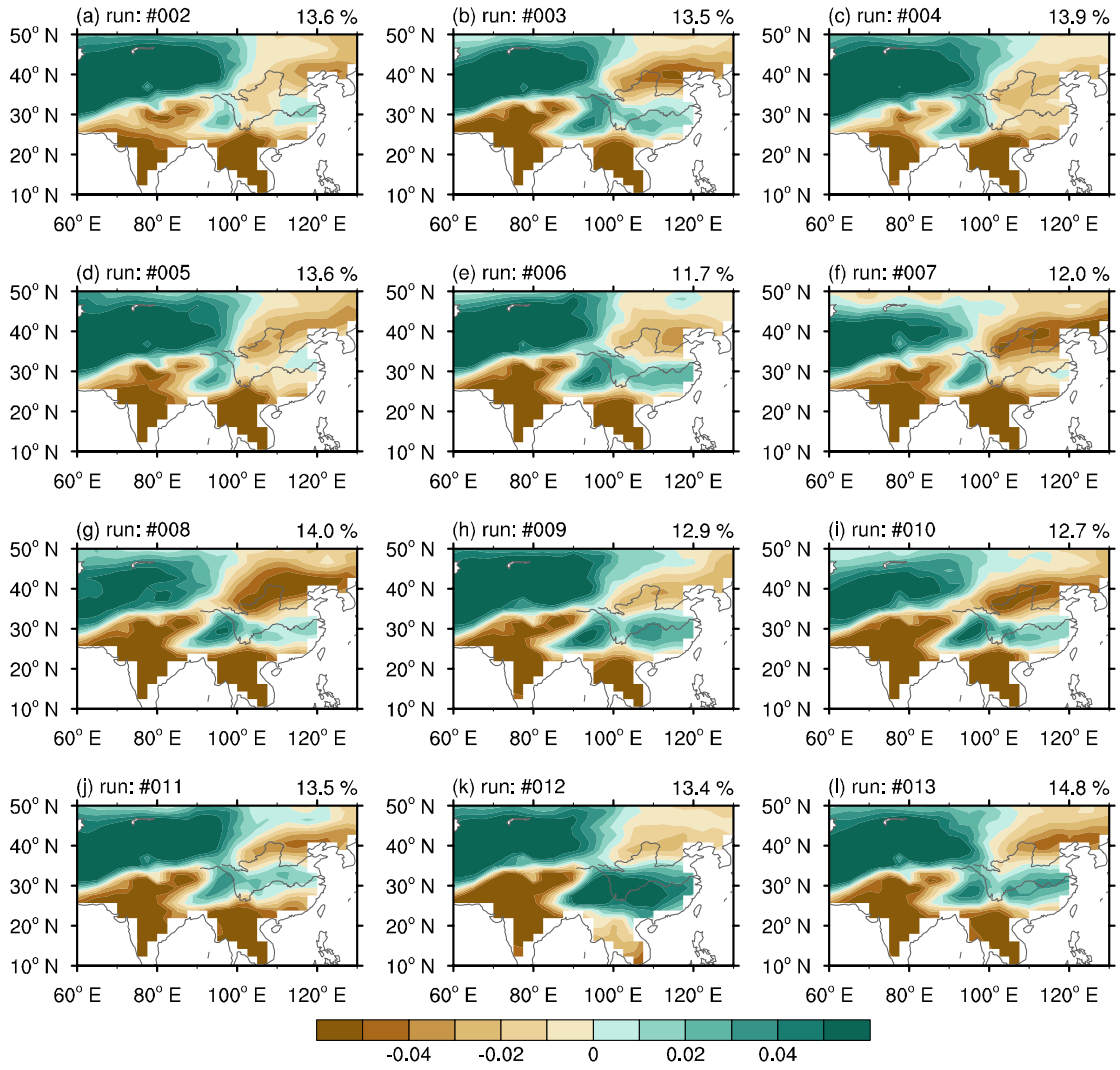

Figure S1. The simulated first leading precipitation mode. **(a–l)** EOF1 of the nine-year low-pass Lanczos filtered annual precipitation in the CESM-LME 12 all-forcing simulations for the time period 850–2005. The explained variances are given at the top-right.

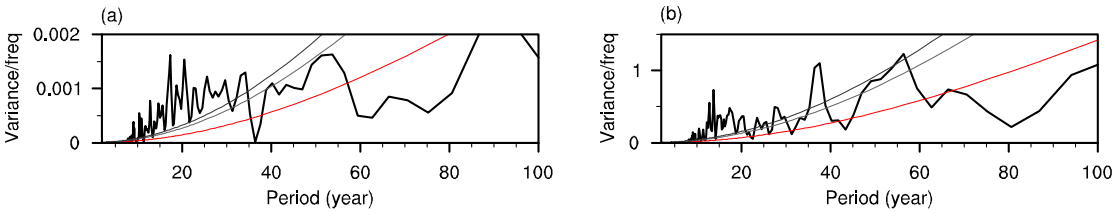

Figure S2. (a) Power spectrum of the time series of the leading decadal precipitation mode (black line) and **(b)** power spectrum of the time series of the IPO index (black line) in the Last Millennium Reanalysis dataset. The dark (light) gray line indicates the confidence curve at the 95% (90%) confidence level and the red line shows the Markov red noise spectrum.

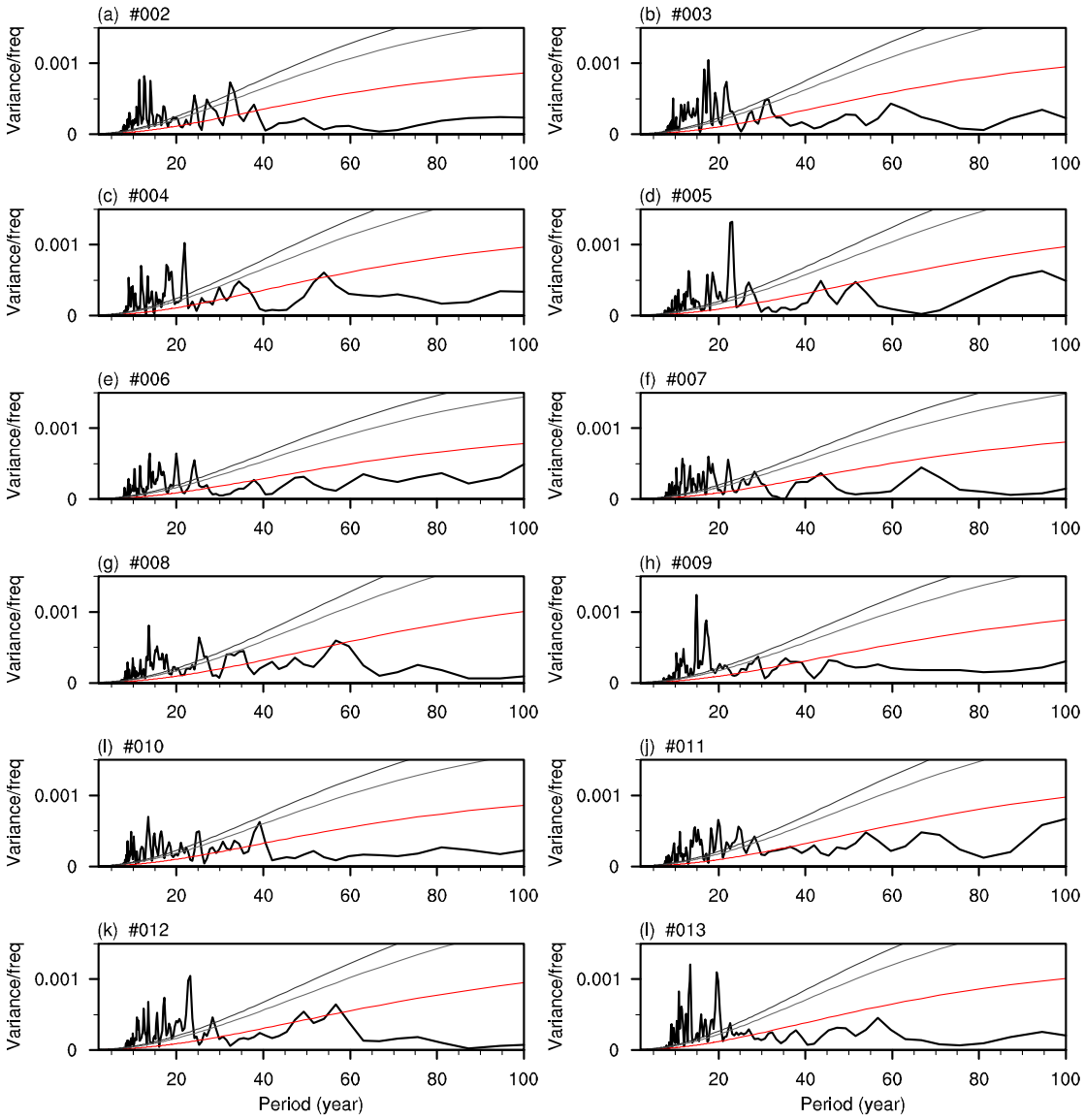

Figure S3. Power spectrum of the time series of the leading decadal precipitation mode (black lines) in the CESM-LME 12 all-forcing simulations. The dark (light) gray lines indicate the confidence curve at the 95% (90%) confidence level and the red lines show the Markov red noise spectrum.

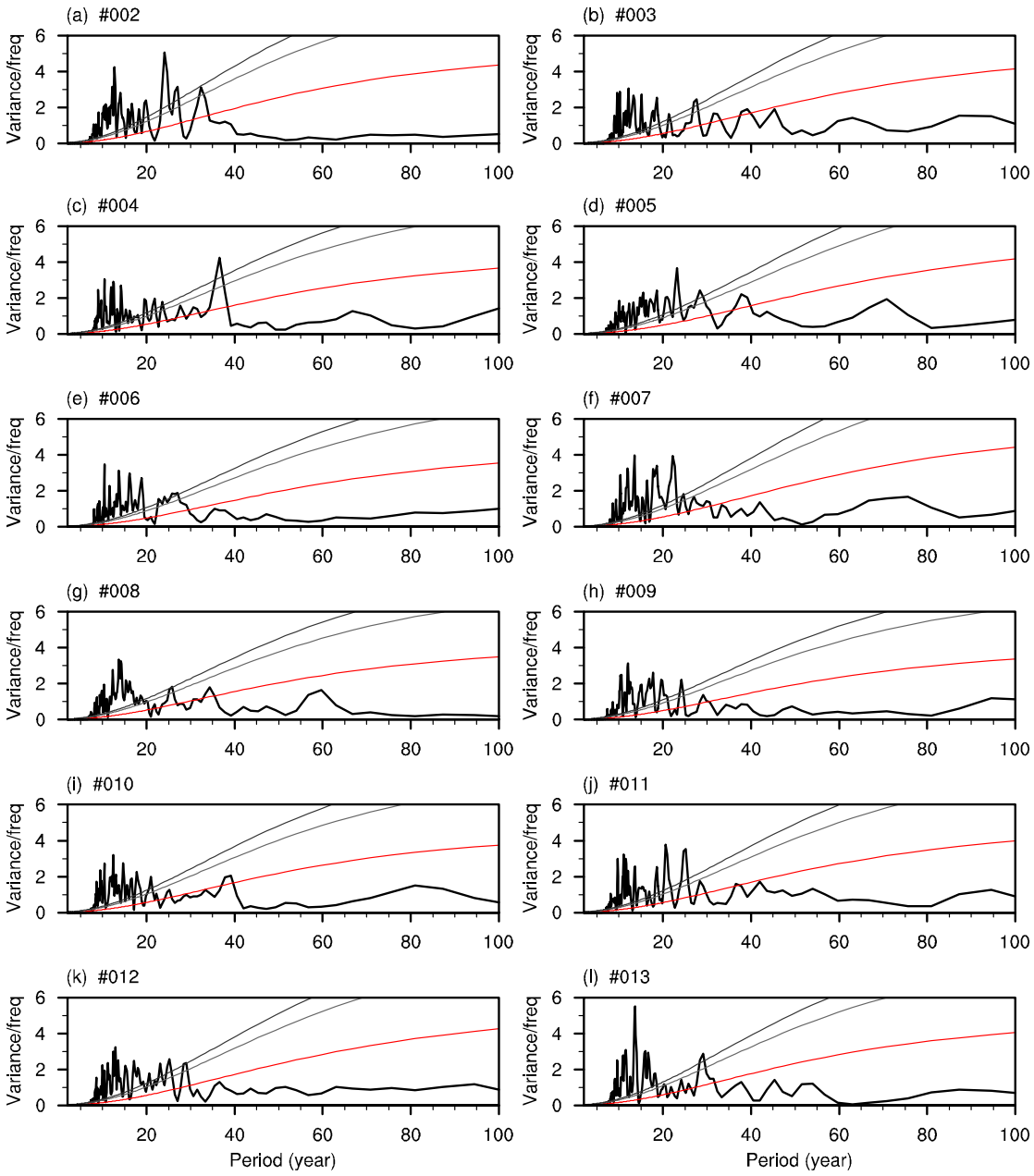

Figure S4. Power spectrum of the time series of the IPO index (black lines) in the CESM-LME 12 all-forcing simulations. The dark (light) gray lines indicate the confidence curve at the 95% (90%) confidence level and the red lines show the Markov red noise spectrum.

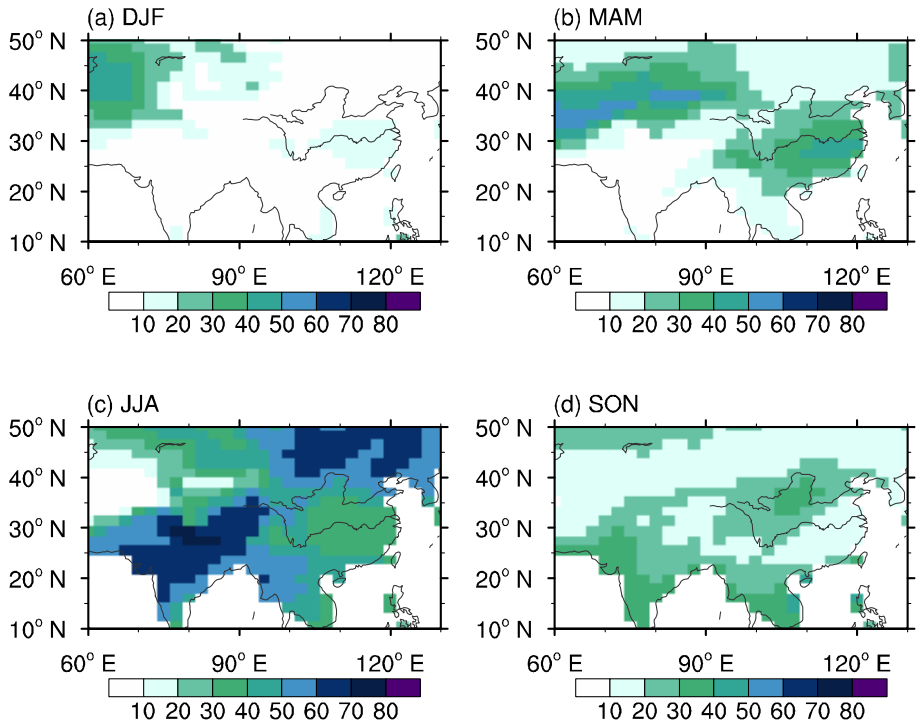

Figure S5. Average values of the percentage of the annual precipitation accounted for by **(a)** winter, **(b)** spring, **(c)** summer and **(d)** autumn precipitation in the CESM-LME all-forcing simulations.

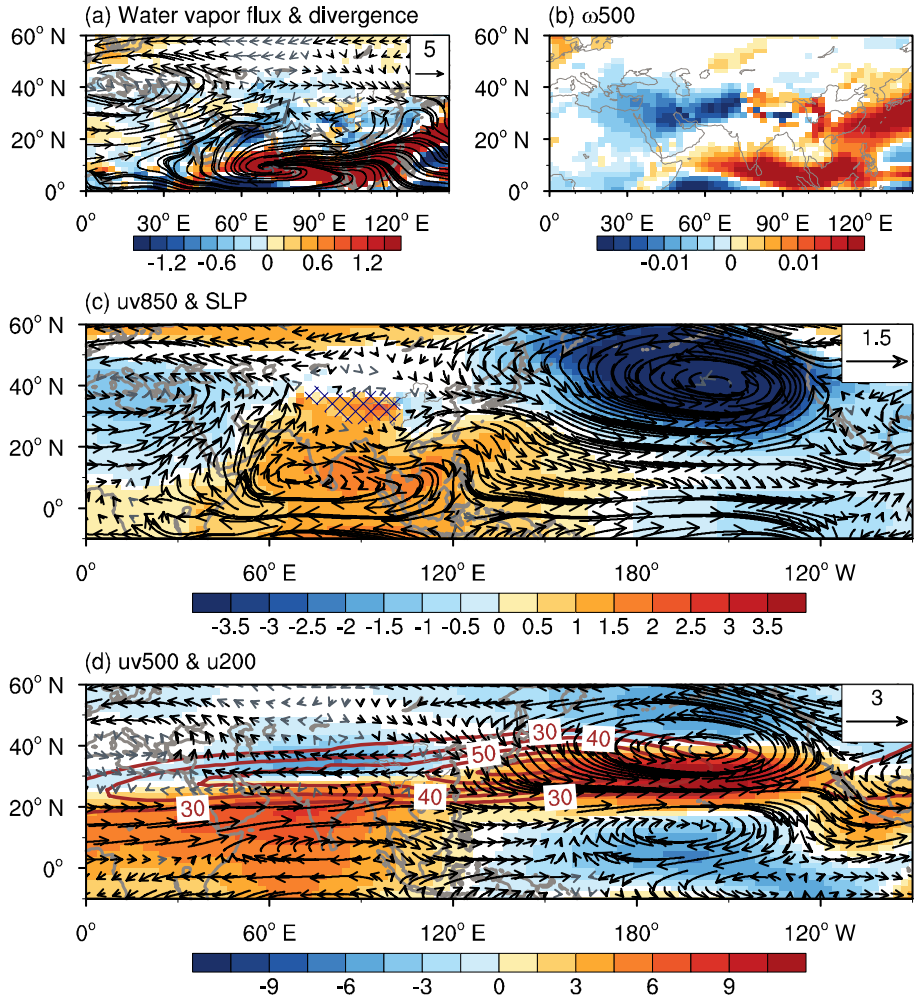

Figure S6. Simulated winter atmospheric circulation anomalies during the positive phases of the IPO. Regressed maps of anomalous **(a)** vertically integrated water vapor flux from 1000 to 300 hPa (vectors; units: kg m^{-1} s^{-1}) and its divergence (shading; units: 10^{-5} kg m^{-2} s^{-1}), **(b)** 500 hPa vertical velocity (ω500) (units: Pa s^{-1}), **(c)** 850 hPa wind (uv850) (vectors; units: m s^{-1}) and SLP (shading; units: hPa), **(d)** 500 hPa wind (uv500) (vectors; units: m s^{-1}) and 200 hPa zonal wind (u200) (shading; units: m s^{-1}) onto the time series of the IPO index simulated by the CESM-LME all-forcing runs. The blue hatched patterns in part **(c)** indicate the region with an altitude >3000 m. The brown contours in part **(d)** are the climatological 200 hPa zonal wind (units: m s^{-1}). The shading shows that the significant anomalies at the 95% confidence level simulated by at least two-thirds of the members agree on the sign of the average. The black vectors show that the significant anomalies at the 95% confidence level simulated by at least two-thirds of the members agree on the sign of the average for the zonal or meridional component.

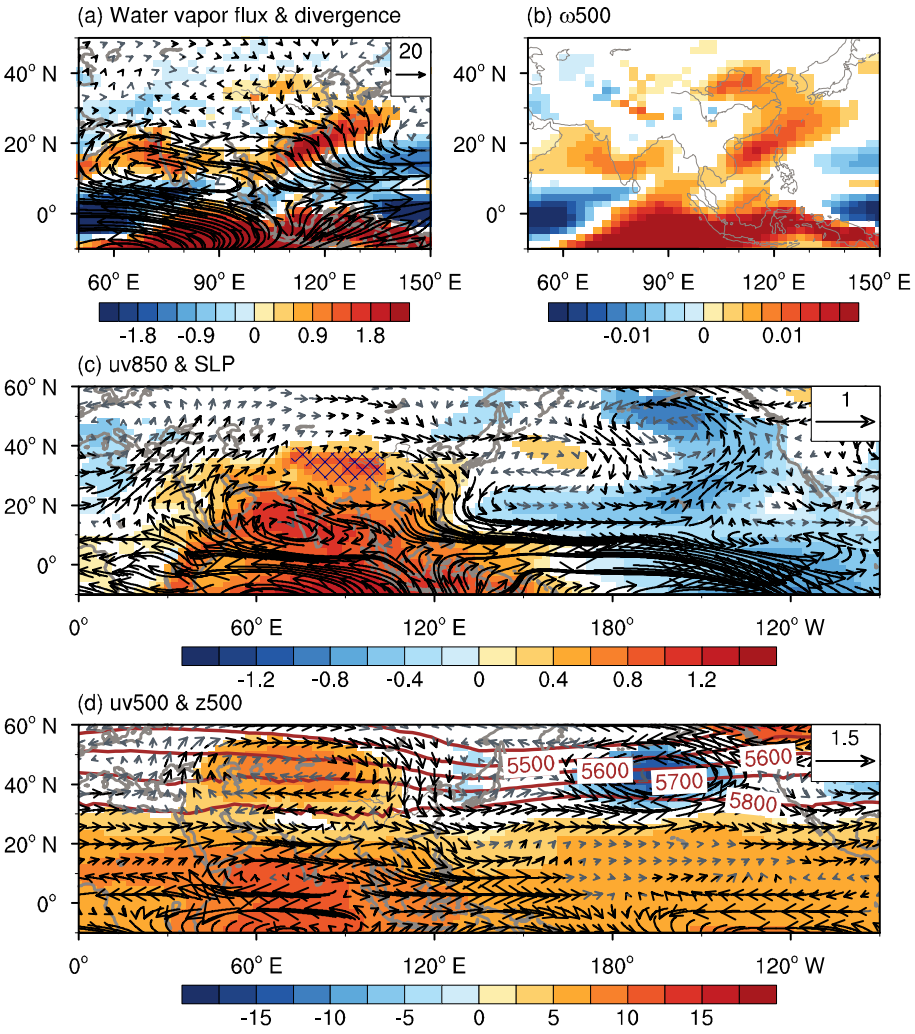

Figure S7. Simulated autumn atmospheric circulation anomalies during the positive phases of the IPO. Regressed maps of anomalous **(a)** vertically integrated water vapor flux from 1000 to 300 hPa (vectors; units: kg m^{-1} s^{-1}) and its divergence (shading; units: 10^{-5} kg m^{-2} s^{-1}), **(b)** 500 hPa vertical velocity (ω500) (units: Pa s^{-1}), **(c)** 850 hPa wind (uv850) (vectors; units: m s^{-1}) and SLP (shading; units: hPa), and **(d)** 500 hPa wind (uv500) (vectors; units: m s^{-1}) and 500 hPa geopotential height (z500) (shading; units: m) onto the time series of the IPO index simulated by the CESM-LME all-forcing runs. The blue hatched patterns in part **(c)** indicate the region with an altitude >3000 m. The brown contours in part **(d)** are the climatological 500 hPa geopotential height (units: m). The shading shows that the significant anomalies at the 95% confidence level simulated by at least two-thirds of the members agree on the sign of the average. The black vectors show that the significant anomalies at the 95% confidence level simulated by at least two-thirds of the members agree on the sign of the average for the zonal or meridional component.

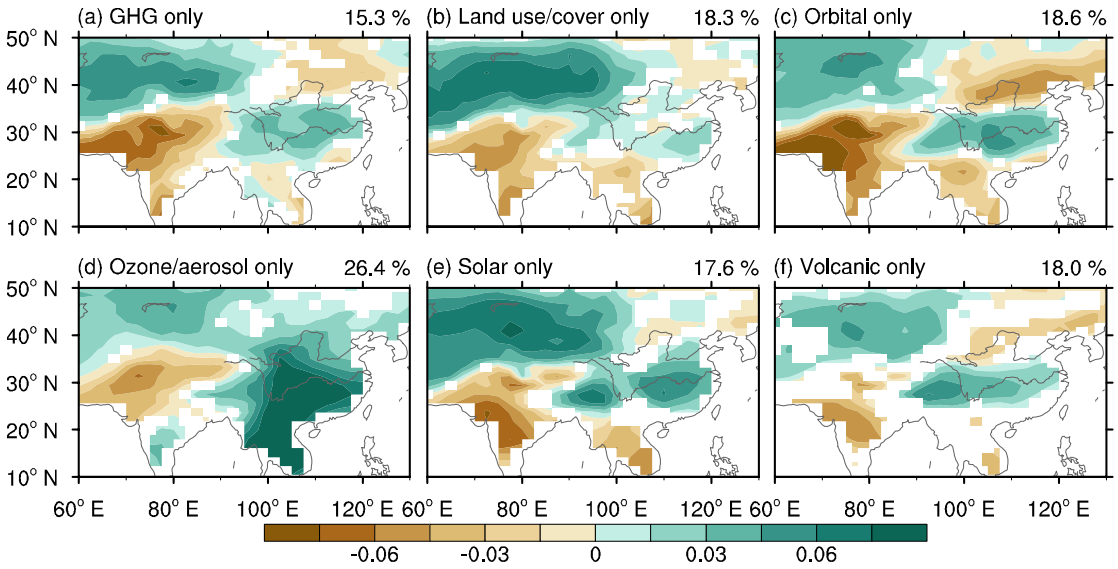

Figure S8. The leading decadal precipitation mode for the time period 1850–2005 in the single-forcing simulations. **(a–f)** The average EOF1 of the nine-year low-pass Lanczos filtered annual precipitation in six subsets of the single-forcing simulations. The averaged explained variance is given at the top-right. The shading shows where at least two-thirds of the members agree on the sign of the average of multiple members.

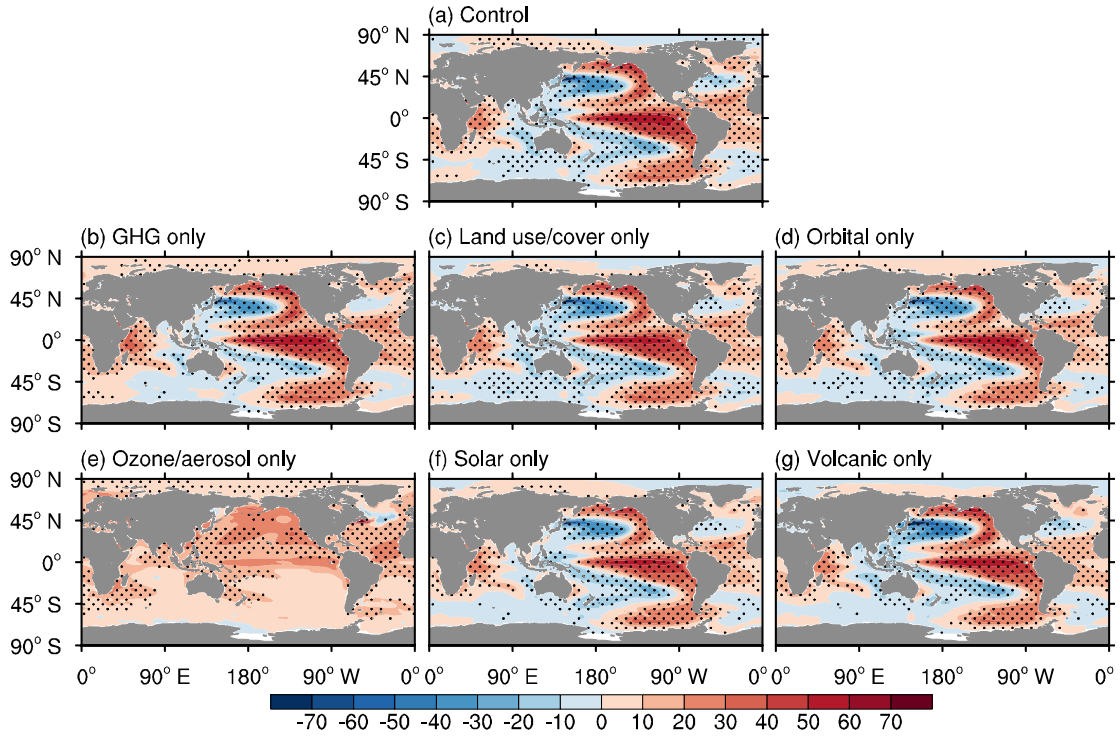

Figure S9. The SST anomalies (units: °C) regressed onto the time series of the leading decadal precipitation mode in the **(a)** control simulation and **(b–g)** six subsets of the single-forcing simulations. The dots in part **(a)** show significant anomalies at the 95% confidence level and the dots in parts **(b–g)** denote that the significant anomalies at the 95% confidence level simulated by at least two-thirds of the members agree on the sign of the average value.

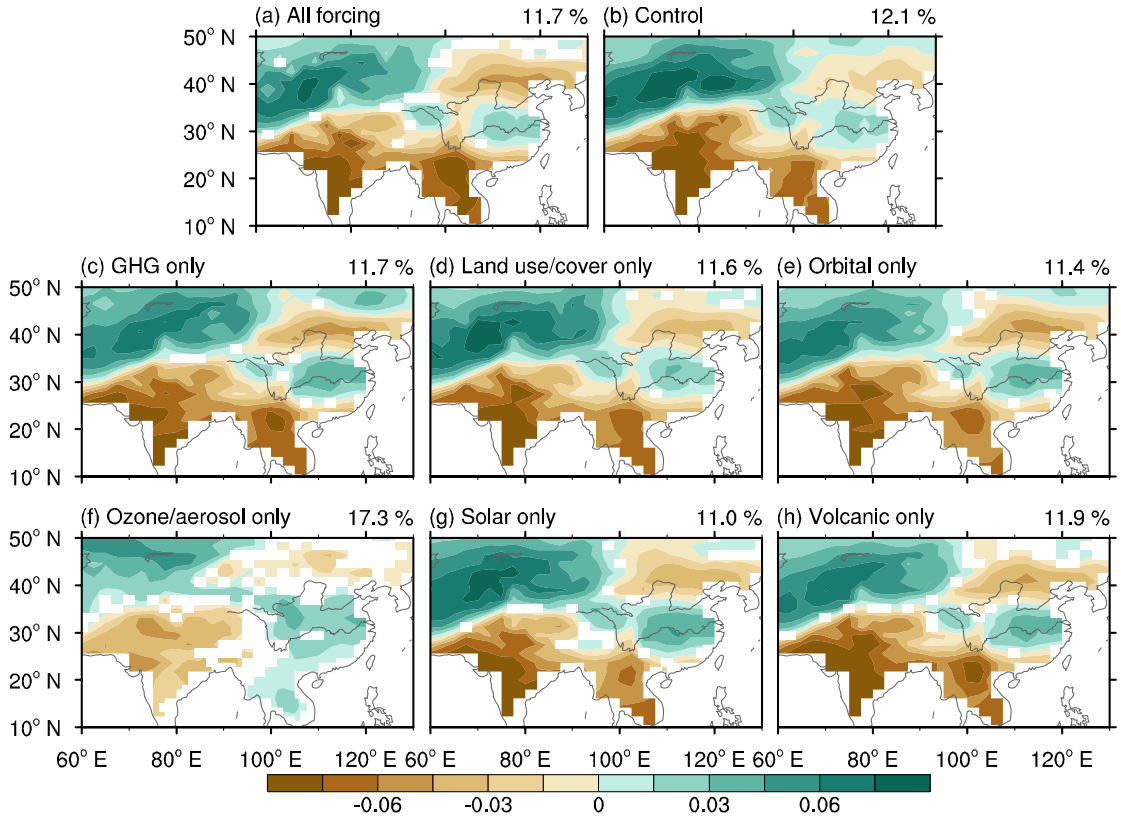

Figure S10. The simulated leading decadal soil moisture mode for the time period 850–2005. **(a)** The average EOF1 of the nine-year low-pass Lanczos filtered soil moisture content (top 10 cm of soil) in the all-forcing simulations. The averaged explained variance is given at the top-right. **(b)** EOF1 of the nine-year low-pass Lanczos filtered soil moisture content in the control simulation. The explained variance is given at the top-right. **(c–h)** The average EOF1 of the nine-year low-pass Lanczos filtered soil moisture content in six subsets of the single-forcing simulations. The averaged explained variance is given at the top-right. The shading in parts **(a, c–h)** shows where at least two-thirds of the members agree on the sign of the average of multiple members.

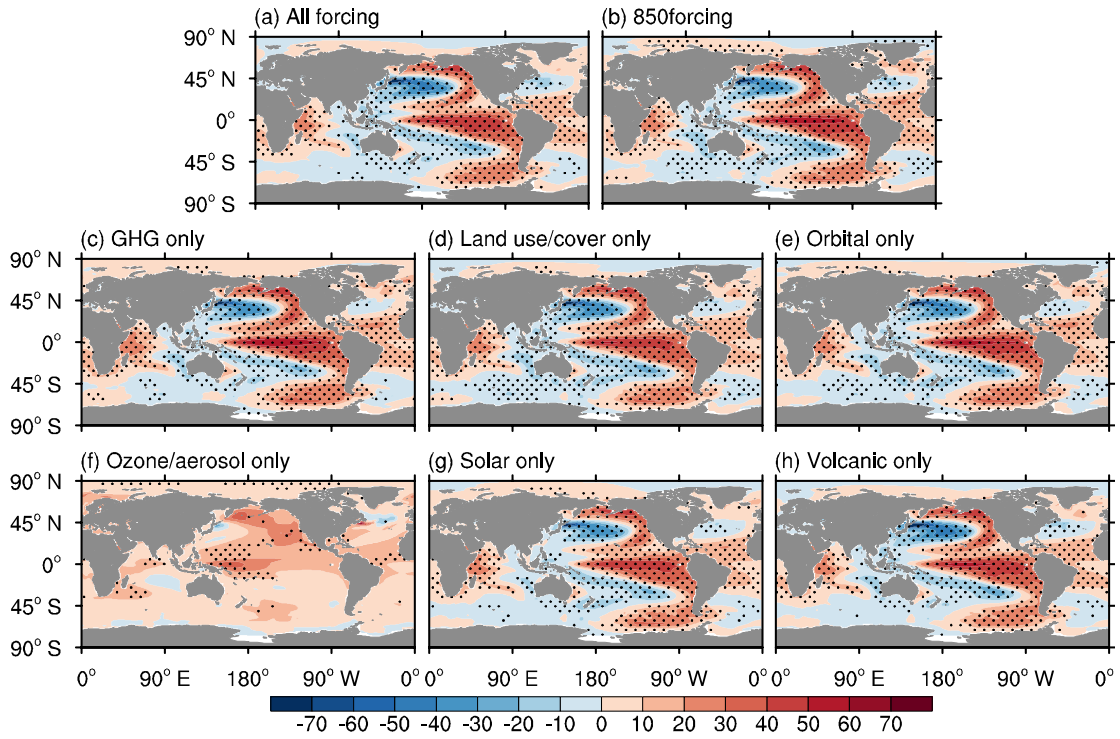

Figure S11. The SST anomalies (units: °C) regressed onto the time series of the leading decadal aridity index mode in the **(a)** all-forcing simulations, **(b)** control simulation, and **(c–h)** six subsets of the single-forcing simulations. The dots in part **(b)** show significant anomalies at the 95% confidence level and the dots in parts **(a, c–h)** denote that the significant anomalies at the 95% confidence level simulated by at least two-thirds of the members agree on the sign of the average value.

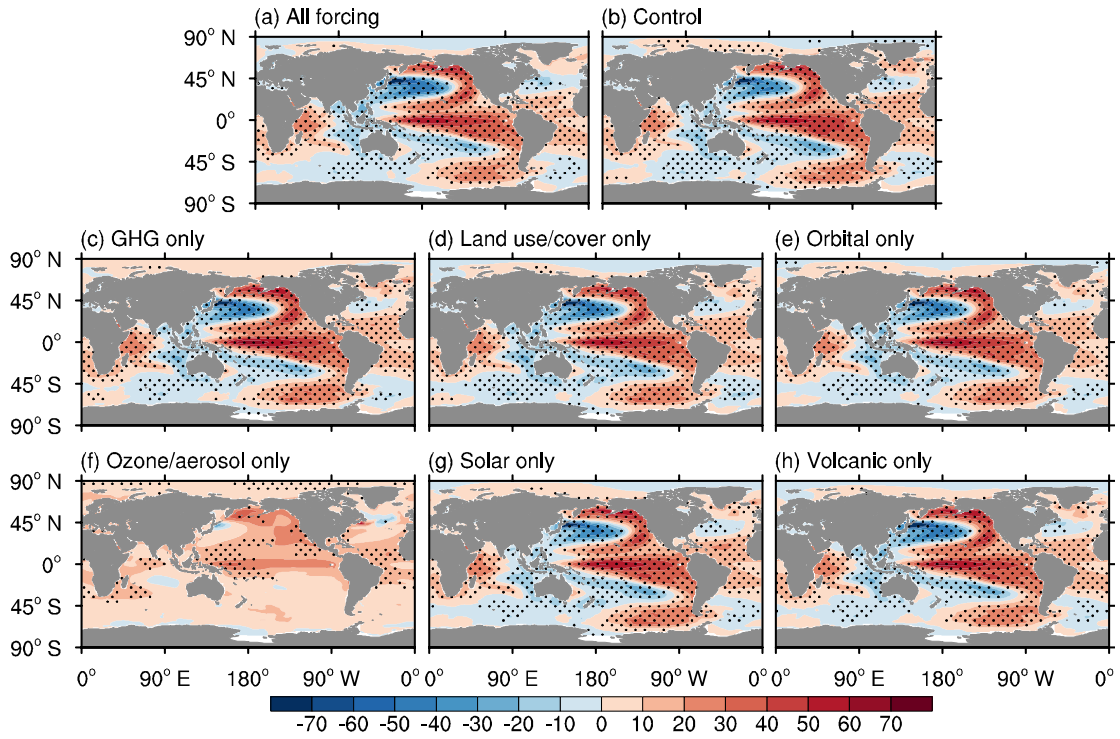

Figure S12. The SST anomalies (units: °C) regressed onto the time series of the leading decadal soil moisture mode in the **(a)** all-forcing simulations, **(b)** control simulation, and **(c–h)** six subsets of the single-forcing simulations. The dots in part **(b)** show significant anomalies at the 95% confidence level and the dots in parts **(a, c–h)** denote that the significant anomalies at the 95% confidence level simulated by at least two-thirds of the members agree on the sign of the average value.

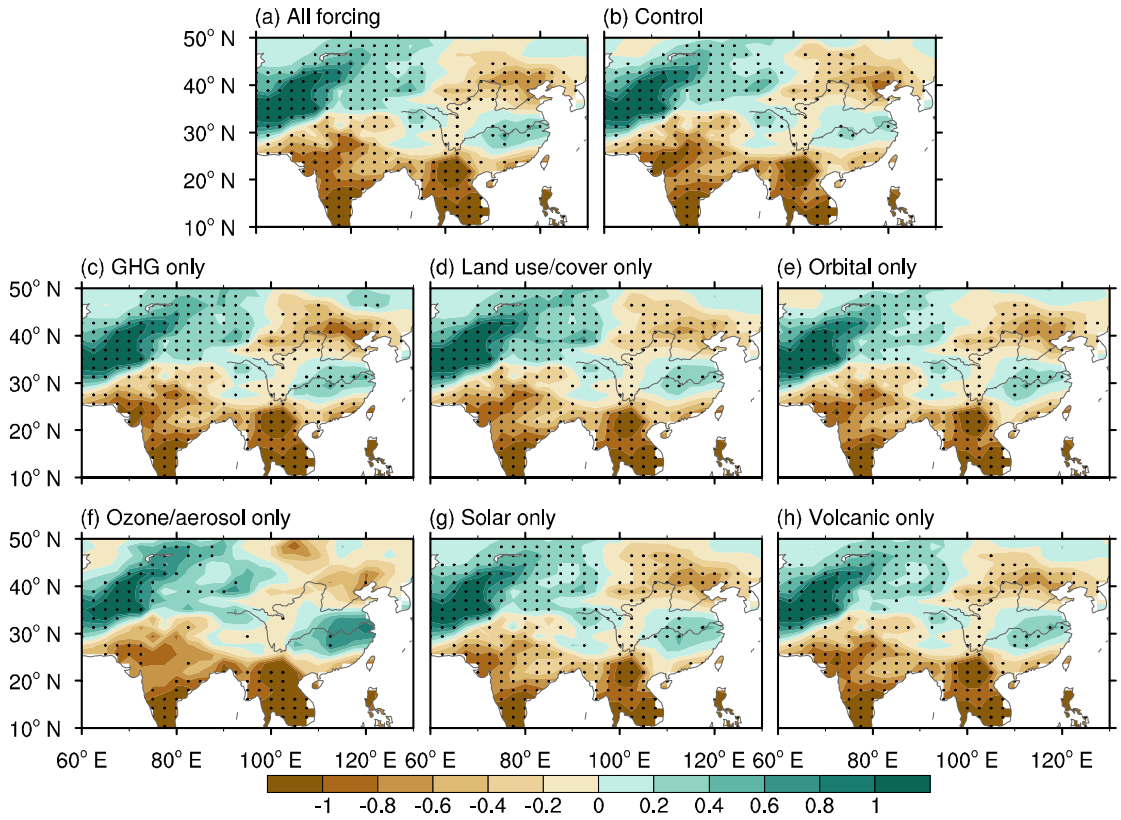

Figure S13. Simulated soil moisture anomalies during the positive phases of the IPO. The soil moisture anomalies (units: kg m^{-2}) regressed onto the time series of the IPO index in the **(a)** all-forcing simulations, **(b)** control simulation, and **(c–h)** six subsets of the single-forcing simulations. The dots in part **(b)** show significant anomalies at the 95% confidence level and the dots in parts **(a, c–h)** denote that the significant anomalies at the 95% confidence level simulated by at least two-thirds of the members agree on the sign of the average value.